DNA-Directed Self-Assembly of Core-Satellite Plasmonic Nanostructures: A Highly Sensitive and Reproducible Near-IR SERS Sensor

*Yuanhui Zheng, Thibaut Thai, Philipp Reineck, Ling Qiu, Yueming Guo, and Udo Bach**

The excitation of surface plasmons in metallic nanostructures provides an opportunity to localize light at the nanoscale, well below the scale of the wavelength of the light. The high local electromagnetic field intensities generated in the vicinity of the nanostructures through this nanofocusing effect are exploited in surface enhanced Raman spectroscopy (SERS). At narrow interparticle gaps, so-called hot-spots, the nanofocusing effect is particularly pronounced. Hence, the engineering of substrates with a consistently high density of hot-spots is a major challenge in the field of SERS. Here, a simple bottom-up approach is described for the fabrication of highly SERS-active gold core-satellite nanostructures, using electrostatic and DNA-directed self-assembly. It is demonstrated that well-defined core-satellite gold nanostructures can be fabricated without the need for expensive direct-write nanolithography tools such as electron-beam lithography (EBL). Self-assembly also provides excellent control over particle distances on the nanoscale. The as-fabricated core-satellite nanostructures exhibit SERS activities that are superior to commercial SERS substrates in signal intensity and reproducibility. This also highlights the potential of bottom-up self-assembly strategies for the fabrication of complex, well-defined functional nanostructures with future applications well beyond the field of sensing.

1. Introduction

Since its initial discovery in the 1970s,[1] surface-enhanced Raman spectroscopy (SERS) has become a powerful tool for the sensing of chemical and biological compounds.[2,3] SERS effects are typically observed on metallic (e.g., gold, silver, and copper) nanostructures, such as metal layers with nanoscale roughness,[4,5] and metal nanoparticles[6,7] and their aggregates.[8–11] The interaction of these nanostructures with light results in the collective oscillation of free electrons in the nanostructures, described as surface plasmons. Surface-plasmon-induced electric-field enhancements can be observed in the close vicinity of metal-nanoparticle surfaces. These enhancements are particularly strong at nanoscopically sharp corners[6,7] and interparticle gaps,[12,13] typically referred to as "hot-spots". The SERS intensity (I_{SERS}) is proportional to the modulus of the localized electromagnetic field squared at the location of the analyte molecule. More specifically:

$$I_{SERS} \propto |E|^2 \propto |gE_0|^2 \quad (1)$$

where $|E|$ and $|E_0|$ are the magnitudes of the localized and incident electromagnetic fields, respectively, and g is the optical gain factor.[14] Metal-nanoparticle assemblies with nanosized spacing (e.g., nanodimers) have shown *E*-field enhancement at hot-spots as high as $\approx 10^5$,[13] enabling SERS signals to be detected with single-molecule sensitivity.[9] The strength of the electric-field enhancement provided by a given plasmonic nanostructure can be fine-tuned by tailoring the metal-nanoparticle shape,[15] interparticle separation,[9] and assembly configuration.[16–23] This also provides the means to adjust the wavelength at which surface plasmon resonance occurs. Tight control over these parameters is a paradigm for the fabrication of highly sensitive and reproducible near-IR-responsive SERS sensors. However, this remains challenging due to the lack of simple nanofabrication methods that provide adequate control of the resulting assembly geometry over large areas (typically several mm^2).

Generally, complex metallic nanostructures with a high SERS activity can either be fabricated by top-down nanolithography techniques or by bottom-up self-assembly approaches. Nanolithography tools such as electron-beam lithography (EBL)[16–18] and focused-ion-beam (FIB) milling[19] allow for the production of customized metallic nanostructures with controllable size,

Dr. Y. H. Zheng, T. Thai, P. Reineck, L. Qiu, Y. M. Guo, Prof. U. Bach
Department of Materials Engineering
Monash University
Wellington Road, Clayton, Victoria 3800, Australia
E-mail: udo.bach@monash.edu
Dr. Y. H. Zheng, T. Thai, Prof. U. Bach
The Melbourne Centre for Nanofabrication
151 Wellington Road, Clayton, Victoria 3168, Australia
Prof. U. Bach
Commonwealth Scientific and Industrial Research Organization
Materials Science and Engineering
Clayton South, Victoria 3169, Australia

DOI: 10.1002/adfm.201202073

shape, spacing, and positioning. A major drawback of these direct-writing techniques is their low output, hampering their use in commercial fabrication processes. Furthermore, it is difficult to control feature sizes below 5 nm, a size-domain that is particularly attractive for the generation of plasmonic hot-spots. Bottom-up approaches, on the other hand, take advantage of self-assembly processes to construct complex metallic nanostructures from individual-metal-nanoparticle building blocks that can be readily synthesized with controlled sizes and shapes through chemistry routes.[20–22]

Metal-nanoparticle arrays have been fabricated through one-step convective,[24] electrostatic,[25] and DNA-directed[26] self-assembly of metal nanoparticles. Among these, the DNA-based approach is the most powerful for the control over the assembly architectures, owing to its programmable self-recognition property.[9,10,27–35] The DNA-directed self-assembly of core-satellite nanostructures from colloidal building blocks was first demonstrated in 1998.[36] Recently, the groups of both Singamaneni and Tsukruk adopted a similar strategy that exploits electrostatic driving forces to produce core-satellite structures in solution, by means of a one-step electrostatic self-assembly process.[37,38] The latter group also developed a cross-linking strategy that involves an esterification and a click reaction to fabricate solvent-born bimetallic core-satellite nanostructures.[39] An alternative fabrication process was presented by Kim et al., based on a two-step assembly process combining electrostatic and biotin-streptavidin lock-key interactions[10] to produce SERS hot-spots which can be reversibly tuned with aptamers.

Herein, we describe a novel hierarchical self-assembly strategy for the fabrication of dense arrays of core-satellite metal nanostructures for their application as SERS substrates. Similar core-satellite metal nanostructures have recently been shown to exhibit high SERS activity.[18] In contrast to our work, these structures were fabricated by means of nanolithographic methods. In this paper we present a low-cost, non-lithographic, scalable method to produce SERS-active core-satellite nanostructures using colloidal metal nanoparticles as building blocks. We study their optical properties and their SERS activities using benzenethiol as a model analyte. Making SERS measurements of surface adsorbed species is important in a range of bioanalytical applications.[40–42] The core-satellite nanostructures exhibit highly reproducible, near-IR responsive SERS signals and Fano like resonances, typically observed in lithographically fabricated metal nanostructures.[16–18]

2. Results & Discussion

To produce a dense array of core-satellite metal nanostructures we have adopted a hierarchical self-assembly strategy, as illustrated schematically in **Scheme 1**. Commercially available, spherical gold nanoparticles (AuNPs) with an average diameter of 30 nm and 20 nm were functionalized with monothiolated DNA (denoted as AuNP/DNA conjugates)[43,44] and used as core and satellite nanoparticle building blocks. The hierarchical self-assembly process involves the electrostatic assembly of 30 nm AuNPs (core-AuNPs), followed by the specific DNA-directed assembly of 20 nm AuNPs onto the core nanoparticles. In order to confer a positive surface charge onto glass slides, they are immersed into an ethanolic solution containing 3-aminopropyltriethoxysilane (APTES) (step 1). The resulting amino-terminated surface is positively charged at neutral and lower pH.[45] Exposing APTES-modified glass slides to a solution of negatively charged core-AuNP/DNA conjugates (step 2) results in core-AuNP adsorption onto the APTES-modified surface. In the subsequent DNA-directed assembly step, we aim to immobilize 20 nm satellite AuNPs specifically around the core-AuNPs. However, prior to the DNA-directed assembly, it is essential to neutralize the remaining positive surface charges to avoid non-specific electrostatic assembly of the negatively charged 20 nm satellite AuNP/DNA conjugates onto the surface of the glass slide. This is accomplished by reacting the slide

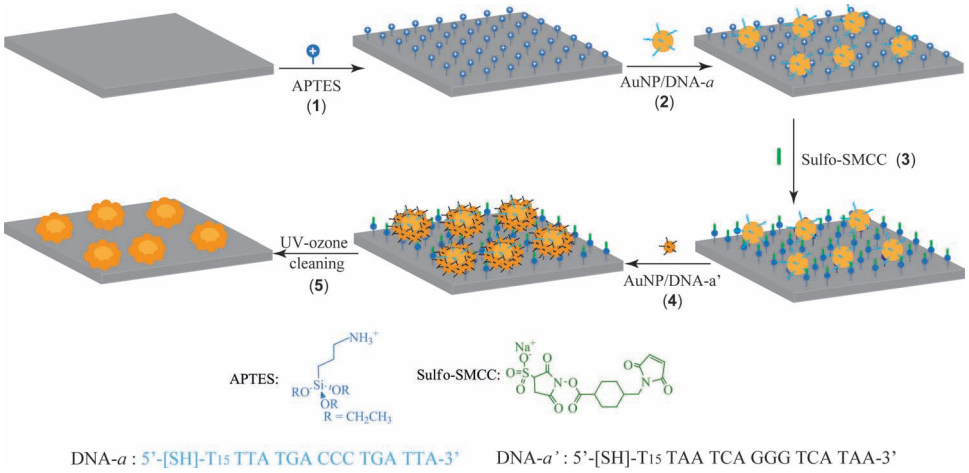

Scheme 1. A schematic representation of the hierarchical self-assembly procedure for the fabrication of core-satellite plasmonic nanostructures: 1) APTES functionalization of a glass substrate; 2) electrostatic immobilization of 30 nm AuNP-DNA conjugates onto the APTES-modified substrate surface; 3) neutralization of surface-confined amino groups by the formation of covalent amide bonds with sulfo-SMCC; 4) hybridization of 20 nm AuNP-DNA conjugates onto the 30 nm AuNPs, forming the core-satellite nanoparticle assemblies; and 5) removal of the surface-confined molecules through UV-ozone cleaning, yielding pristine gold surfaces.

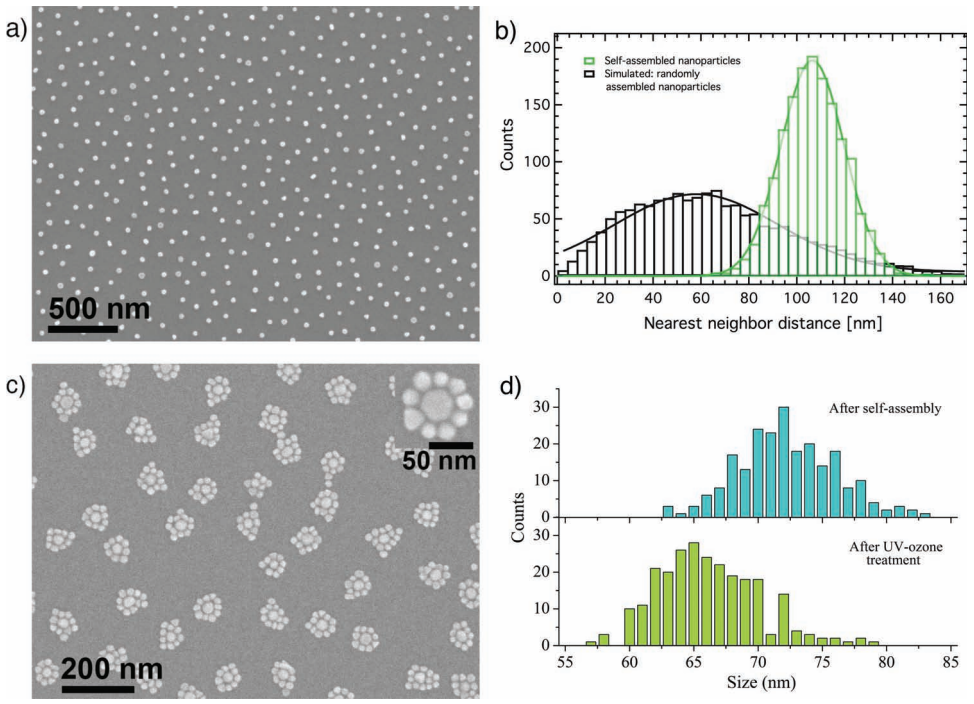

Figure 1. SEM micrographs and statistical analysis: a) SEM micrograph of an array of core AuNPs (30 nm diameter) on a silicon substrate fabricated through electrostatic self-assembly. b) Distance analysis of the nanoparticles shown in panel (a): The distance between each core-AuNP and its nearest neighbor was measured (center-to-center) using image analysis (grey bars). The nearest-neighbor-distance distribution simulated for the same number of particles per area, but randomly placed, is shown for comparison (black bars). Fit: Gaussian function. See Supporting Information for details. c) SEM micrographs of an array of core-satellite nanostructures on a silicon substrate obtained by immobilization of 20 nm satellite AuNPs onto the core-AuNPs shown in panel (a) through DNA-directed self-assembly. d) A statistical analysis of the size distribution of the core-satellite nanostructures prior to and after UV-ozone treatment. An example of the size calculation for the core-satellite nanostructures prior to and after UV-ozone treatment is shown in Supporting Information, Figure S3.

with sulfosuccinimidyl-4-[*N*-maleimidomethyl]cyclohexane-1-carboxylate (sulfo-SMCC) (step 2). Its amine-reactive *N*-hydroxysuccinimide (NHS ester) functionality readily reacts with the surface-confined amino groups, forming a neutral amide bond. Subsequently the slides are exposed to the satellite AuNPs, which carry a DNA sequence complementary to that on the core-AuNPs, yielding the desired core-satellite nanostructures (step 3). UV-ozone treatment following the successful self-assembly is directed at removing all surface-confined molecules to obtain pristine gold surfaces (step 4) ready to adsorb analytes for their detection in SERS experiments. Further experimental details are provided in the Experimental Section.

Controlling the distance between the core-AuNPs on the substrate is essential: it needs to be large enough to ensure that individual core-satellite structures are separated while keeping it as small as possible to obtain a high surface coverage. The former guarantees a narrow optical response of non-interacting core-satellite structures, while the latter maximizes light absorption. The core-AuNP surface density can be precisely controlled by adjusting the self-assembly conditions, such as the average number of DNA strands adsorbed on each AuNP, the AuNP concentration, and the ionic strength of the aqueous medium. **Figure 1**a shows the result of the electrostatic self-assembly process for core-AuNPs from ultrapure water. The distance between each core-AuNP and its nearest neighbor was determined via image analysis for a large number of particles (>1500). The histogram exhibits a very narrow distribution of nearest neighbor distances (NNDs) (Figure 1b, grey bars) around an average NND of 106 nm, with a standard deviation of only 13 nm.

A simple simulation model was used to generate random particle distributions with the same number of particles placed on the same area. Here, the analysis shows a very wide spread in NNDs (37 nm standard deviation) with an average NND of 66 nm, emphasizing the fact that the self-assembly process is not stochastic (see Supporting Information for details). This can be rationalized in terms of the electrostatic repulsion of surface-confined nanoparticles and nanoparticles in solution. An AuNP approaching the substrate surface is attracted by the positively charged amino groups on the APTES-modified surface, but also repelled by the electric field that arises from the negative charges located on already adsorbed AuNPs. Additional nanoparticles can only adsorb onto the surface where this repulsive force is overcome by the attractive force to the APTES-modified surface. This explains the larger average NND of 106 nm determined for the controlled self-assembly compared with the stochastic case. Figure 1c shows a typical scanning electron microscopy (SEM) micrograph of the resulting core-satellite nanostructures following steps 1–4 described in Scheme 1. Interestingly, the core-satellite nanostructures all appear to adapt a planar configuration where the satellite particles are located in close vicinity to the substrate. This phenomenon has

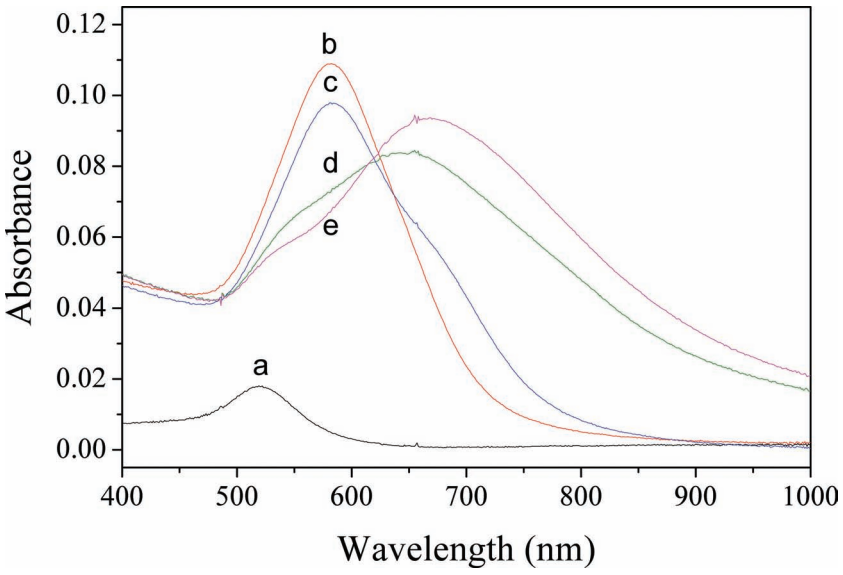

Figure 2. Absorption spectra of the self-assembled AuNPs on glass substrates: core-AuNPs only (a), core-satellite Au-NP structures directly after the DNA-directed self-assembly of the satellite particles (b), core-satellite Au-NP structures after MCH treatment (c), core-satellite Au-NP structures after UV-ozone treatment (d); Au-NP core-satellite structures after benzenethiol loading (e).

also been observed by other groups when drying solution-born core-satellite nanostructures on transmission electron microscopy (TEM) grids.[36,37] From a purely statistical perspective, the self-assembly in solution should allow the attachment of satellite-particles to the core-AuNPs from all accessible space angles. Post-assembly conformational changes during the drying step driven by capillary forces can explain the formation of the planar particle arrangement observed in the SEM images. The statistical image analysis of a 2.6 μm × 2.2 μm section on the substrate (see Supporting Information, Figure S2) shows that 72% of the core-AuNPs formed individual core-satellite structures, while the remaining 28% formed merged satellite structures mostly containing two core particles. An average of 9.5 satellite AuNPs assembled around each core while less then 0.5% of the satellite particles adsorbed non-specifically (not in the direct vicinity of a core-AuNP) onto the APTES-modified substrates. This indicates that the chemical conversion of surface-confined positively charged amino groups with sulfo-SMCC to neutral amides was successful. It should be noted that sulfo-SMCC is typically used as a bifunctional cross-linker. In addition to the sulfo-NHS ester, it also contains a cyclohexane maleimide functionality, which in our approach is not expected to undergo any further reaction during the self-assembly process. The bulkiness of this group is likely to further impede surface adsorption of satellite AuNPs through van der Waals interactions. The absence of any detectable SERS signal following the subsequent UV-ozone treatment also provides clear evidence that the maleimide functionality is quantitatively removed prior to exposure to the Raman reporter molecule, benzenethiol. Alternative monofunctional NHS-esters have also been successfully used for the APTES passivation step, yet sulfo-SMCC proved to be marginally more efficient in avoiding non-specific adsorption of the satellite AuNPs. SEM images obtained prior to and following UV-ozone cleaning (see Supporting Information, Figure S3) show that there was no significant geometry change during the UV-ozone treatment. A statistical analysis of the core-satellite-assembly sizes before and after UV-ozone treatment, however, indicates an average decrease in the distance between the core- and satellite-nanoparticle surfaces of approximately 3 nm (Figure 1d).

The optical properties of the core-satellite AuNP assemblies on glass substrates were recorded using transmission UV–vis absorption spectroscopy at different stages of the self-assembly process. The surface immobilized core-AuNPs show similar optical properties to their colloidal aqueous solutions, exhibiting a distinct plasmon absorption peak at 525 nm (**Figure 2**a). Upon self-assembly of the satellite-nanoparticles, the maximum absorption of the sample increases by 5.5 times, accompanied by a red shift of the absorption peak to 580 nm (Figure 2b). The optical properties of EBL-predefined core-satellite nanostructures have previously been investigated and modeled in depth by other groups.[16–18] Red-shifted absorption peaks and Fano like resonances have been predicted and experimentally observed. Fano like resonances typically show a double peak separated by a characteristic sharp minimum. Experimental extinction spectra of a plasmonic octamer core-satellite nanostructures fabricated via EBL showed that the Fano like resonances can also be evidenced as a shoulder in the absorption spectrum.[16–18] The same group also observed the evolution of a red-shifted absorption peak, as the distance between satellite and center particles is decreased. In our approach we expected that the AuNP-confined DNA, necessary to direct the assembly of core and satellite nanoparticles, would act as a spacer layer that defines a minimum gap between the nanoparticles following the drying step. However, due to the denaturation and loss of the hydration shell upon drying, this spacer layer will be significantly thinner than what generally would be expected in the solubilized state, for example where DNA is used to define the distance of metal nanoparticles in plasmonic rulers.[46] Exposure of surface-immobilized layers of monothiolated, single-stranded DNA to other thiols has previously been shown to lead to a partial replacement of DNA via a classical thiol exchange reaction.[47] In an attempt to exploit this substitution reaction, we exposed the freshly assembled and dried core-satellite AuNP assemblies to an aqueous solution of 6-mercapto-1-hexanol (MCH). Films treated with MCH typically showed the appearance of a shoulder in the absorption spectrum at around 680 nm (Figure 2c), indicating stronger coupling between the nanoparticles and a narrowing of interparticle gaps within the assemblies.[16,18] The UV-ozone treatment caused a significant red-shift of the absorption maximum of more than 50 nm. This can be attributed to a stronger plasmonic coupling between individual particles and is in good qualitative agreement with the 3 nm decrease in interparticle distance between core- and satellite nanoparticles as determined in the SEM image

analysis. The exposure of the core-satellite AuNP assemblies to the Raman reporter molecule (benzenethiol) results in a slight red-shift of the plasmon resonances (Figure 2e) due to an increase in the refractive index of the local dielectric environment of the nanoparticles.[17]

In order to evaluate the SERS performance of the core-satellite AuNP assemblies, benzenethiol was adopted as a model analyte. **Figure 3**a compares the Raman spectra of benzenethiol adsorbed on three different substrates: the core-satellite AuNP assemblies, a commercial Klarite SERS substrate, and 30 nm core-AuNPs. All of the substrates were excited at a wavelength of 782 nm. Strong Raman signals at 417, 691, 999, 1022, 1073 and 1573 cm^{-1}, originating from benzenethiol,[48] were observed for the core-satellite AuNP assemblies and Klarite SERS substrate but not for the core-AuNPs. An excellent correlation between the peak positions and the relative intensities of the two Raman spectra was observed for benzenethiol when adsorbed on the core-satellite AuNP and the Klarite substrates. The signal-to-noise ratios (SNRs) for the Raman peak at 1075 cm^{-1} are 69 and 18 for the core-satellite AuNP assemblies and the Klarite SERS substrate, respectively. The SNR for the core-satellite AuNP assemblies was 3.8 times higher than that for the Klarite SERS substrate. The broad, weak Raman peak near 1400 cm^{-1}, a signature of P=O double bonds,[49] was observed for the core-AuNPs without MCH treatment, but not for the core-satellite AuNP assemblies with MCH treatment (see Supporting Information, Figure S4). The exposure to a MCH solution is a critical step to minimize the formation of oxygen-containing phosphorous compounds on the surface of core-satellite AuNP assemblies during the subsequent UV-ozone treatment, thus enhancing the SERS signals of the Raman reporter molecule.

High SERS activity and near-field enhancement for similar core-satellite nanostructures defined by the EBL technique have previously been reported.[18] The observed SERS signal strengths strongly correlate with the electric-field enhancement calculated for the interparticle hot-spots within such assemblies.[18] Continuous-wave laser excitation at a wavelength of 782 nm was found to yield significantly stronger SERS signals compared with a 514 nm or 633 nm wavelength excitation, despite the fact that the overall excitation energy flux was lowest for the 782 nm excitation condition (see Supporting Information, Figure S5). The high SERS activity at 782 nm is in good agreement with a recent theoretical and experimental SERS study on EBL-defined core-satellite nanostructures, where the highest near-field enhancement was observed at a wavelength longer than the corresponding maximum surface resonance wavelength.[18]

Good reproducibility of the SERS response is crucial for the design of reliable sensors that allow quantification of a specific analyte. We therefore undertook a statistical analysis to quantify the variation in the SERS signal intensity between different locations on one substrate (spot-to-spot variation) and between different substrates (substrate-to-substrate variation). Figure 3b shows the spot-to-spot variation of the SERS signal intensity at the 1075 cm^{-1} peak for a core-satellite substrate as well as for a commercial Klarite SERS substrate. Both were exposed overnight to a 1.0×10^{-6} M solution of benzenethiol. More than thirty individual spots were characterized for each substrate. The average signal intensity for the core-satellite substrate was 12 900 counts with a coefficient of variation of 15%. For comparison,

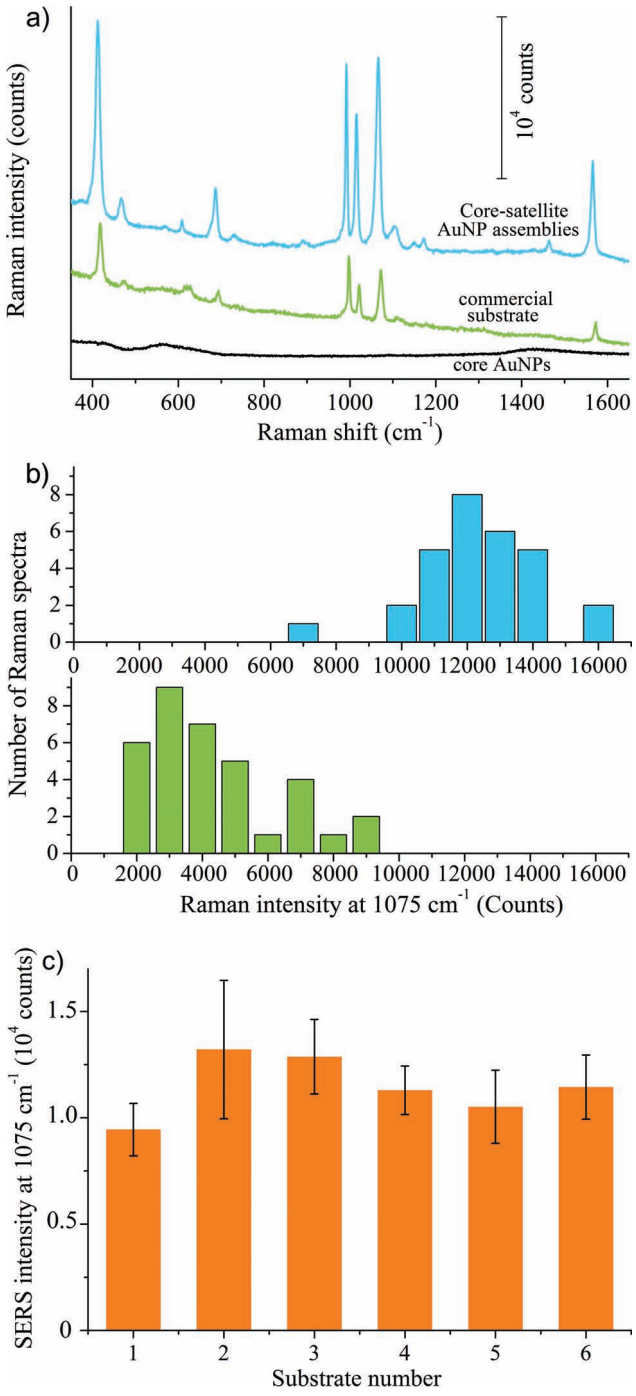

Figure 3. a) SERS spectra of benzenethiol adsorbed on the core-satellite AuNP assemblies (blue line) on glass substrates, fabricated through a sequence of electrostatic and DNA-directed self-assembly steps, a commercial Klarite SERS substrate (green line) and 30 nm core-AuNPs only (black line), excited at 782 nm. b) The spot-to-spot SERS intensity variation at 1075 cm^{-1} for the core-satellite AuNP assemblies (blue bars) and a commercial Klarite SERS substrate (green bars). c) Substrate-to-substrate SERS intensity variation at 1075 cm^{-1} measured for six different substrates. Each intensity value represents the average of ten measurements at different spots. The standard deviations (i.e., the spot-to-spot variability for each sample) are shown as error bars. For all of these samples, the benzenethiol-loading concentration and time are 1×10^{-6}M and 12 h, respectively.

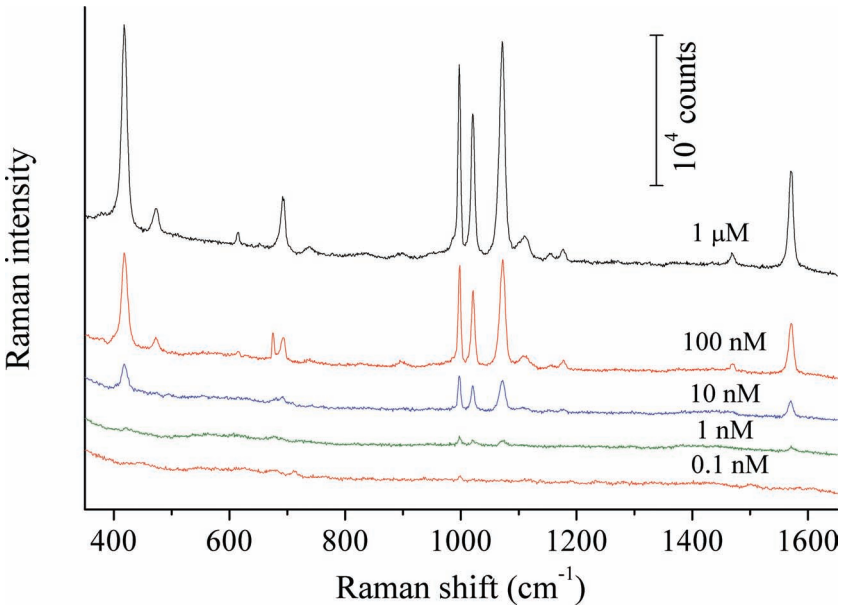

Figure 4. SERS spectra of benzenethiol adsorbed on the core-satellite AuNP assemblies on glass substrates as a function of benzenethiol-loading concentration.

the commercial substrate yielded an average signal intensity of 4350 counts and a coefficient of variation of 45%, indicating a better signal reproducibility for the core-satellite substrate. In order to examine the substrate-to-substrate variation, we studied the SERS activity of six core-satellite substrates that resulted from independent self-assembly processes. For each substrate the 1075 cm^{-1} Raman peak height was measured at ten different spots. The average signal height for each substrate is plotted in Figure 3c. The average signal count over the six substrates is 11 500 counts with a coefficient of variation of 12%. This indirectly reconfirms that the self-assembly process presented here provides excellent control over the assembly parameters such as the surface density of core-satellite structures, as well as the interparticle gap within each assembly as both of these strongly affect the overall SERS activity of the sample.

To determine the detection limit of the core-satellite AuNP assemblies, the SERS substrates were exposed overnight to benzenethiol solutions varying in concentration between 10^{-10}–10^{-6} M. **Figure 4** shows the SERS spectra of these samples. As expected, the Raman signals of the benzenethiol decrease with decreasing benzenethiol-loading concentration. The SERS peaks at 999, 1022, and 1075 cm^{-1} can be clearly observed down to a benzenethiol concentration of 1×10^{-9} M, while the spectral fingerprint of benzenethiol almost disappears for the substrate exposed to a 1×10^{-10} M solution. The SNRs for these Raman peaks were determined to be 3.1, 1.7, and 2.0, respectively, for the 1×10^{-9} M benzenethiol loading solution, yielding a detection limit below 1×10^{-9} M.

Conclusions

In conclusion, we have demonstrated a novel, two-step self-assembly strategy for the scalable low-cost fabrication of complex core-satellite AuNP assemblies. In recent studies, similar core-satellite metal nanostructures have been fabricated using nanolithography techniques.[16–18] Their high SERS activity has been explained in terms of the presence of hot-spots located at interparticle gaps within the assembly.[18] Here, we demonstrate that well-defined core-satellite metal nanostructures can be fabricated without the need for expensive direct-write nanolithography tools such as EBL. Self-assembly also provides excellent control over nanosized interparticle distances. The as-fabricated core-satellite nanostructures exhibited SERS activities that were superior to commercial SERS substrates in signal intensity and reproducibility. The amount of DNA necessary to achieve a dense coverage of core-satellite metal nanostructures over 1 m^2 was calculated to be 0.42 nmol (see Supplementary Information). Assuming a typical cost for small-scale customized DNA synthesis of US$2.00 per nmol the overall DNA cost to cover 1 m^2 would be less than $1.00, showing the commercial viability of DNA-directed fabrication techniques for the production of nanosensors. Chemical synthesis offers nearly unlimited control over the size, shape, and composition of metal-nanoparticle building blocks, while DNA-directed self-assembly strategies allow for the development of complex assembly processes, far beyond the simple two-step process reported here. This work represents a simple proof-of-concept experiment leading the way to a plethora of nanostructures with tailored properties towards applications such as sensing and photovoltaics. SERS-active metal nanostructures, functionalized with probe molecules sensitive to local environmental conditions have recently also been used successfully to map properties such as pH[40] and redox potentials,[42] both in vitro and in vivo at micrometer resolution. This opens up an additional exciting new field of applications for functional nanostructures as the core-satellite structures presented here. Further increases in the SERS enhancement factor, by increasing the light scattering of the core-satellite nanostructures, are currently in progress, targeting the development of highly reproducible near-IR SERS sensors with detection limits down to the single molecular level. This can be achieved through the use of larger metal nanoparticles and/or high refractive-index substrates (e.g., silica-coated silicon substrates).

Experimental Section

Synthesis of AuNP-DNA Conjugates: Commercially available AuNPs (20 nm and 30 nm diameter) were functionalized with monothiolated DNA according to a method described earlier.[36,37] In a typical procedure, 1 mL of citrate-stabilized solution (Ted Pella) with an optical density of 1.0 was concentrated from 1 mL to 100 μL by centrifugation (4000 rpm, 45 min). 5 μL of 2.0% polyoxyethylene (20) sorbitan monolaurate (Tween 20) (Sigma–Aldrich), 30 μL of 0.1 M phosphate buffer (pH = 7.0), 50 μL of 2.0 M NaCl, a given volume of 100×10^{-6} M particle DNA solution (30 nm AuNPs: 20 μL; 20 nm AuNPs: 10 μL) and 5 μL of 100×10^{-3} M

bis(p-sulfonateophenyl)phenylphosphine dihydrate dipotassium (BSPP) (Sigma–Aldrich) were added to the AuNP solution. The particle DNA strands were purchased from Fidelity Systems Inc. and their sequences were 5′-[HS]-T_{15}-TTA TGA CCC TGA TTA-3′ (denoted as DNA-*a*) and 5′-[HS]-T_{15}-TAA TCA GGG TCA TAA-3′ (denoted as DNA-*a′*). The mixture was incubated at room temperature overnight; the AuNP/DNA colloidal solution was washed three times with ultrapure water. After the final washing step, the 30 nm AuNP/DNA-*a* conjugates were redispersed in 1 mL of ultrapure water ([AuNP] ≈ 0.33×10^{-9} M), while the 20 nm AuNP/DNA-*a′* were redispersed in 200 µL of a buffer ([AuNP] ≈ 5.8×10^{-9} M) of 0.05% Tween 20, 0.5 M NaCl, and 20×10^{-3} M K_2HPO_4/KH_2PO_4 (pH = 7.0).

APTES Modification of Silicon and Glass Substrates: A silicon (4 mm × 6 mm) or glass (12 mm × 13 mm) substrate was modified with a layer of APTES by immersion into a mixture of APTES, water, and ethanol at volume ratio of 2:3:95 for 1 h, washed with ethanol three times, dried under a stream of nitrogen, and baked at 110 °C for 10 min.

Synthesis of Core-Satellite Nanostructures: In a typical procedure, a given volume (20 µL for silicon substrate and 50 µL for glass substrate) of the 30 nm AuNP-DNA-*a* solution was placed on an APTES-modified silicon or glass surface and incubated in a humidity chamber for 2 h. The substrate was washed three times with ultrapure water to remove non-specifically adsorbed AuNPs, and dried under a stream of nitrogen. The substrate was subsequently immersed into 2 mL of buffered sulfo-SMCC solution containing 2.0×10^{-3} M sulfo-SMCC and 10×10^{-3} M phosphate buffer (pH = 7.5) at 45 °C for 2 h to neutralize the surface charges of the amino groups. Following the sulfo-SMCC treatment, the substrate was washed three times with ultrapure water and then placed in a centrifuge tube containing 200 µL of the 20 nm AuNP/DNA-*a′* solution. The tube was placed in a 65 °C water bath that was allowed to slowly reach room temperature and incubated for 12 h, upon which the substrate was washed with a buffered saline solution containing 0.5 M NaCl and 20×10^{-3} M K_2HPO_4/KH_2PO_4 (pH = 7.0), as well as a 0.1 M ammonium acetate solution three times, respectively, and then dried naturally in air. Subsequently, the substrate was exposed to a 1×10^{-3} M 6-mercapto-1-hexanol (MCH) saline solution ([NaCl] = 5.0 M) for 1 h, washed with a buffered saline solution containing 0.5 M NaCl and 20×10^{-3} M K_2HPO_4/KH_2PO_4 (pH = 7.0), as well as a 0.1 M ammonium acetate solution three times, respectively, and then dried under a stream of nitrogen. Following the MCH treatment, the substrate was exposed to UV-ozone at an oxygen flow rate of 3 L min^{-1} for 3 × 20 min. After the UV-ozone treatment, the substrate was immersed in 2 mL of different concentrations (i.e., 1×10^{-10}, 1×10^{-9}, 1×10^{-8}, 1×10^{-7} and 1×10^{-6} M) of benzenethiol in ethanol solution and left for 12 h, upon which the substrate was rinsed with ethanol and then dried under a stream of nitrogen. For comparison, the core-AuNPs and a commercial Klarite SERS substrate was exposed to UV ozone and benzenethiol under the same conditions as the core-satellite AuNP assemblies prior to the SERS measurements.

Characterization: Scanning electron microscopy (SEM) images of the self-assembled core-satellite nanostructures were taken with a field-emission SEM (JEOL 7001 F). Since conductive substrates are required for the SEM measurements, silicon substrates were used as supporting substrates for the self-assembly of the core-satellite nanostructures. For Raman and optical measurements, transparent glass slides were used as supporting substrates for the self-assembly of the core-satellite nanostructures. Absorption spectra were recorded using an Agilent 8453 UV–vis spectrometer. Raman spectra were recorded using a Renishaw RM 2000 Confocal micro-Raman System equipped with a near-IR diode laser at a wavelength of 782 nm (laser power: 1.15 mW and laser spot-size: 1 µm). All of the Raman spectra were collected by fine-focusing a 50× microscope objective and the data acquisition time was 10 s.

Supporting Information

Supporting Information is available from the Wiley Online Library or from the author.

Acknowledgements

Dr. Finley Shanks, Dr. Ryo Sekine and Prof. Don McNaughton are acknowledged for technical assistance with the Raman spectroscopic measurements. The authors acknowledge financial support from the Australian Research Council through an Australian Research Fellowship (UB). Further financial support has been received from Commonwealth Scientific and Industrial Research Organization through an OCE Science Leader position (UB). This work was performed in part at the Melbourne Centre for Nanofabrication, an initiative partly funded by the Commonwealth of Australia and the Victorian Government.

Received: July 24, 2012
Revised: September 4, 2012
Published online: October 22, 2012

[1] a) M. Fleischmann, P. J. Hendra, A. J. McQuillan, *Chem. Phys. Lett.* **1974**, *26*, 163; b) D. L. Jeanmaire, R. P. Van Duyne, *J. Electroanal. Chem.* **1977**, *84*, 1; c) M. G. Albrecht, J. A. Creighton, *J. Am. Chem. Soc.* **1977**, *99*, 5215.
[2] J. N. Anker, W. P. Hall, O. Lyandres, N. C. Shah, J. Zhao, R. P. Van Duyne, *Nat. Mater.* **2008**, *7*, 442.
[3] S. Lal, S. Link, N. J. Halas, *Nat. Photonics* **2007**, *1*, 641.
[4] V. Prokopec, J. Cejkova, P. Matějka, P. Hasal, *Surf. Interface Anal.* **2008**, *40*, 601.
[5] H. Li, C. E. Baum, J. Sun, B. M. Cullum, *Appl. Spectrosc.* **2006**, *60*, 1377.
[6] S. Boca, D. Rugina, A. Pintea, L. Barbu-Tudoran, S. Astilean, *Nanotechnology* **2011**, *22*, 055702.
[7] H. Liang, Z. Li, W. Wang, Y. Wu, H. Xu, *Adv. Mater.* **2009**, *21*, 4614.
[8] J. M. McLellan, Z. Y. Li, A. R. Siekkinen, Y. Xia, *Nano Lett.* **2007**, *7*, 1013.
[9] D. K. Lim, K. S. Jeon, H. M. Kim, J. M. Nam, Y. D. Suh, *Nat. Mater.* **2010**, *9*, 60.
[10] N. H. Kim, S. J. Lee, M. Moskovits, *Adv. Mater.* **2011**, *23*, 4152.
[11] V. Liberman, C. Yilmaz, T. M. Bloomstein, S. Somu, Y. Echegoyen, A. Busnaina, S. G. Cann, K. E. Krohn, M. F. Marchant, M. Rothschild, *Adv. Mater.* **2010**, *22*, 4298.
[12] J. Nelayah, M. Kociak, O. Stéphan, F. J. G. de Abajo, M. Tencé, L. Henrard, D. Taverna, I. Pastoriza-Santos, L. M. Liz-Marzán, C. Colliex, *Nat. Phys.* **2007**, *3*, 348.
[13] E. Hao, G. C. Schatz, *J. Chem. Phys.* **2004**, *120*, 357.
[14] H. Ko, S. Singamaneni, V. V. Tsukruk, *Small* **2008**, *4*, 1576.
[15] A. Kinkhabwala, Z. F. Yu, S. H. Fan, Y. Avlasevich, K. Mullen, W. E. Moerner, *Nat. Photonics* **2009**, *3*, 654.
[16] M. Hentschel, D. Dregely, R. Vogelgesang, H. Giessen, N. Liu, *ACS Nano* **2011**, *5*, 2042.
[17] J. B. Lassiter, H. Sobhani, J. A. Fan, J. Kundu, F. Capasso, P. Nordlander, N. J. Halas, *Nano Lett.* **2010**, *10*, 3184.
[18] J. Ye, F. Wen, H. Sobhani, J. B. Lassiter, P. V. Dorpe, P. Nordlander, N. J. Halas, *Nano Lett.* **2012**, *12*, 1660.
[19] A. Dhawan, M. Gerhold, T. Vo-Dinh, *Nanobiotechnology* **2007**, *3*, 174.
[20] R. G. Freeman, K. C. Grabar, K. J. Allison, R. M. Bright, J. A. Davis, A. P. Guthrie, M. B. Hommer, M. A. Jackson, P. C. Smith, D. G. Walter, M. J. Natan, *Science* **1995**, *267*, 1629.
[21] J. A. Fan, C. Wu, K. Bao, J. Bao, R. Bardhan, N. J. Halas, V. N. Manoharan, P. Nordlander, G. Shvets, F. Capasso, *Science* **2010**, *328*, 1135.
[22] J. A. Fan, Y. He, K. Bao, C. Wu, J. Bao, N. B. Schade, V. N. Manoharan, G. Shvets, P. Nordlander, D. R. Liu, F. Capasso, *Nano Lett.* **2011**, *11*, 4859.

[23] V. Liberman, C. Yilmaz, T. M. Bloomstein, S. Somu, Y. Echegoyen, A. Busnaina, S. G. Cann, K. E. Krohn, M. F. Marchant, M. Rothschild, *Adv. Mater.* **2010**, *22*, 4298.
[24] D. M. Kuncicky, B. G. Prevo, O. D. Velev, *J. Mater. Chem.* **2006**, *16*, 1207.
[25] R. G. Freeman, K. C. Grabar, K. J. Allison, R. M. Bright, J. A. Davis, A. P. Guthrie, M. B. Hommer, M. A. Jackson, P. C. Smith, D. G. Walter, M. J. Natan, *Science* **1995**, *267*, 1629.
[26] J. P. Zhang, Y. Liu, Y. G. Ke, H. Yan, *Nano Lett.* **2006**, *6*, 248.
[27] C. J. Loweth, W. B. Caldwell, X. Peng, A. P. Alivisatos, P. G. Schultz, *Angew. Chem. Int. Ed.* **1999**, *38*, 1808.
[28] M. M. Maye, D. Nykypanchuk, M. Cuisinier, D. van der Lelie, O. Gang, *Nat. Mater.* **2009**, *8*, 388.
[29] F. A. Aldaye, H. F. Sleiman, *J. Am. Chem. Soc.* **2007**, *129*, 4130.
[30] A. J. Mastroianni, S. A. Claridge, A. P. Alivisatos, *J. Am. Chem. Soc.* **2009**, *131*, 8455.
[31] X. Xu, N. L. Rosi, Y. Wang, F. Huo, C. A. Mirkin, *J. Am. Chem. Soc.* **2006**, *128*, 9286.
[32] D. S. Sebba, J. J. Mock, D. R. Smith, T. H. LaBean, A. A. Lazarides, *Nano Lett.* **2008**, *8*, 1803.
[33] J. Sharma, R. Chhabra, A. Cheng, J. Brownell, Y. Liu, H. Yan, *Science* **2009**, *323*, 112.
[34] D. Nykypanchuk, M. M. Maye, D. van der Lelie, O. Gang, *Nature* **2008**, *451*, 549.
[35] S. Y. Park, A. K. R. Lytton-Jean, B. Lee, S. Weigand, G. C. Schatz, C. A. Mirkin, *Nature* **2008**, *451*, 553.
[36] R. C. Mucic, J. J. Storhoff, C. A. Mirkin, R. L. Letsinger, *J. Am. Chem. Soc.* **1998**, *120*, 12674.
[37] N. Gandra, A. Abbas, L. Tian, S. Singamaneni, *Nano Lett.* **2012**, *12*, 2645.
[38] R. Gunawidjaja, E. Kharlampieva, I. Choi, V. V. Tsukruk, *Small* **2009**, *5*, 2460.
[39] R. Gunawidjaja, S. Peleshanko, H. Ko, V. V. Tsukruk, *Adv. Mater.* **2008**, *20*, 1544.
[40] S. W. Bishnoi, C. J. Rozell, C. S. Levin, M. K. Gheith, B. R. Johnson, D. H. Johnson, N. J. Halas, *Nano Lett.* **2006**, *6*, 1687.
[41] G. McNay, D. Eustace, W. E. Smith, K. Faulds, D. Graham, *Appl. Spectrosc.* **2011**, *65*, 825.
[42] C. A. R. Auchinvole, P. Richardson, C. McGuinnes, V. Mallikarjun, K. Donaldson, H. McNab, C. J. Campbell, *ACS Nano* **2012**, *6*, 888.
[43] Y. Zheng, C. H. Lalander, T. Thai, S. Dhuey, S. Cabrini, U. Bach, *Angew. Chem. Int. Ed.* **2011**, *50*, 4398.
[44] C. H. Lalander, Y. Zheng, S. Dhuey, S. Cabrini, U. Bach, *ACS Nano* **2010**, *4*, 6153.
[45] C. H. Kuo, H. Y. Chang, C. P. Liu, S. H. Lee, Y. W. You, J. J. Shyue, *Phys. Chem. Chem. Phys.* **2011**, *13*, 3649.
[46] C. Sönnichsen, B. M. Reinhard, J. Liphardt, A. P. Alivisatos, *Nat. Biotechnol.* **2005**, *23*, 741.
[47] S. Park, K. A. Brown, K. Hamad-Schifferli, *Nano Lett.* **2004**, *4*, 1925.
[48] T. H. Joo, M. S. Kim, K. Kim, *J. Raman Spectrosc.* **1987**, *18*, 57.
[49] F. L. Galeener, J. C. Mikkelsen, *Solid State Commun.* **1979**, *30*, 505.